





Sliding dynamics of a particle in a soap film

Youna Louyer,¹ Benjamin Dollet² , Isabelle Cantat¹ and Anaïs Gauthier¹ 

¹Univ Rennes, CNRS, IPR (Institut de Physique de Rennes) – UMR 6251, F-35000 Rennes, France

²Université Grenoble Alpes, CNRS, LIPhy, 38000 Grenoble, France

Corresponding author: Anaïs Gauthier, anaïs.gauthier@univ-rennes.fr

(Received 3 December 2024; revised 28 January 2025; accepted 2 February 2025)

We investigate the sliding dynamics of a millimetre-sized particle trapped in a horizontal soap film. Once released, the particle moves toward the centre of the film in damped oscillations. We study experimentally and model the forces acting on the particle, and evidence the key role of the mass of the film on the shape of the film and particle dynamics. Not only is the gravitational distortion of the film measurable, it completely determines the force responsible for the motion of the particle – the catenoid-like deformation induced by the particle has negligible effect on the dynamics. Surprisingly, this is expected for all film sizes as long as the particle radius remains much smaller than the film width. We also measure the friction force, and show that ambient air and the film contribute almost equally to the friction. The theoretical model that we propose predicts exactly the friction coefficient as long as inertial effects can be neglected in air (for the smallest and slowest particles). The fit between theory and experiments sets an upper boundary $\eta_s \leq 10^{-8}$ Pa s m for the surface viscosity, in excellent agreement with recent interfacial microrheology measurements.

Key words: bubble dynamics, thin films, wetting and wicking

1. Introduction

Despite their ephemeral nature and apparent fragility, soap bubbles and soap films can withstand large stresses. As first shown by Courbin & Stone (2006) and later by Gilet & Bush (2009), soap films act as non-linear vertical springs (liquid trampolines) capable of repelling a drop or a particle approaching at low velocity. For more violent impacts, they deform so much that they let the incoming object pass without rupturing (Pan & Law 2007; Fell *et al.* 2013). They capture instead a fraction of the particle kinetic energy (Le Goff *et al.* 2008), making foams capable of stopping projectiles. The transition

between bouncing and crossing is governed by the Weber number, which compares the surface energy of the film with the kinetic energy of the particle (Gilet & Bush 2009). Using this criterion, soap films can be used as liquid sieves, trapping the small and slow objects while allowing the larger and faster ones to pass (Stogin *et al.* 2018).

Soap films are usually modelled quasi-statically, considering only the effect of surface tension forces: they are often considered and studied as real-life minimal surfaces (Courant 1940; Almgren & Taylor 1976; Goldstein *et al.* 2010). In presence of a drop or a particle, the expected minimal surface is a catenoid, a geometry that matches relatively well the shape of a film deformed by an impacting object (Gilet & Bush 2009; Chen *et al.* 2019). Experimentally, the weight of the liquid contained in a soap film is not expected to significantly affect its geometry as long as the film dimension does not exceed a characteristic length $\ell \sim \gamma/(\rho g e)$, where γ is the surface tension of the film, e its thickness, ρ the density of the liquid and g gravity (Cohen *et al.* 2017). For a film of thickness $e = 10 \mu\text{m}$, the length ℓ is equal to 30 cm, which is larger than the films usually studied. Here, we consider the dynamics of a millimetre-sized marble trapped in a 10 centimetre-wide horizontal soap film. For this problem, we evidence in contrast the key role of the intrinsic weight of the film, whose deformation is at the origin of the particle motion. We also focus on the drag force experienced by a bead and evidence the almost equal contributions of air and the film.

2. Experiment

A soap film with dimensions $2L \times 2L$ (with $3.3 \text{ cm} \leq L \leq 5 \text{ cm}$) is produced by dipping a square frame in a soap solution consisting of 5.6 g L^{-1} of sodium dodecyl sulfate (SDS), 50 mg L^{-1} of dodecanol in a water–glycerol mixture (15 % of glycerol in volume). The concentration of SDS is more than two times the critical micellar concentration ($\text{CMC}_{\text{SDS}} = 2.37 \text{ g L}^{-1}$), and the surface tension of the film is equal to $\gamma = 33.2 \pm 0.1 \text{ mN m}^{-1}$. Glycerol is used to reduce evaporation so that a film lasts 1–3 min before rupture. To ensure the repeatability of the experiments, the frame is removed from the bath at a constant velocity V_{motor} using a motorised stage. The thickness e of the film is calibrated as a function of V_{motor} , by puncturing the film and following the growth of the hole with a high-speed camera (Phantom Miro LAB3a10) at 6000 f.p.s. The opening velocity V is related to e by the Taylor–Culick law: $e = 2\gamma/(\rho V^2)$ (Taylor 1959; Culick 1960), with $\rho \simeq 1042 \text{ kg m}^{-3}$ the density of the soap solution. The film thickness e is thus varied in a controlled manner between 3 and $25 \mu\text{m}$, with an error of 15 %. In almost all experiments, $V_{\text{motor}} = 20 \text{ cm s}^{-1}$ and a film thickness $e = 9.8 \pm 1.4 \mu\text{m}$ is expected. Approximately 10 s after the film fabrication, a millimetre-sized particle (Silibeads from Sigmund Lindner) with radius R_b ($250 \mu\text{m} \leq R_b \leq 750 \mu\text{m}$), mass m_b and density ρ_b ($2580 \text{ kg m}^{-3} \leq \rho_b \leq 9200 \text{ kg m}^{-3}$) is deposited in the film, a few centimetres from the centre (figure 1a). The particle is initially wet by the soap solution, so that it is held in the film after its release. It is thus surrounded by a meniscus whose height and width increase with time as the liquid in the film is drained towards the bead by capillary suction (Aradian, Raphaël & de Gennes 2001; Guo *et al.* 2019). For a given extension R of the meniscus (relative to the centre of the particle), the shape of the meniscus is fully determined using the model of Orr, Scriven & Rivas (1975) (see figure 5a in Appendix A). The volume and mass of the meniscus can thus be calculated exactly.

Figure 1(b) illustrates the motion of a particle with radius $R_b = 0.5 \text{ mm}$ and mass $m_b = 3.7 \text{ mg}$ after its release in the film without initial velocity. The bead spontaneously slides towards the centre of the film, following a very flattened spiral trajectory (see also supplementary movie 1 at <https://doi.org/10.1017/jfm.2025.157>). The positions x and y of

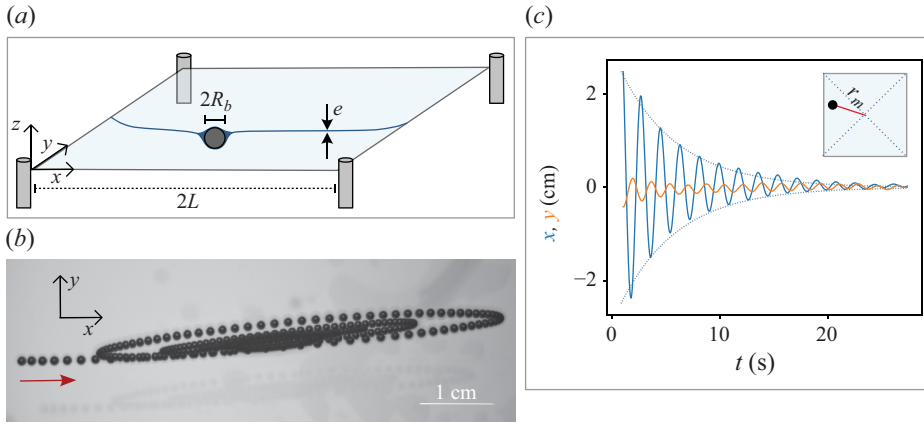


Figure 1. (a) A bead with radius R_b is deposited in a square soap film of size $2L \sim 10$ cm and thickness $e \sim 10 \mu\text{m}$. (b) Top view. Chronophotography showing the trajectory of a bead of mass $m_b = 3.7$ mg (effective mass $m = 4.41$ mg) and radius $R_b = 0.5$ mm within the film, as seen from the top. Two different images of the particle are separated by 20 ms. (c) Position (x, y) of the particle relative to the centre of the film as a function of time t . It follows closely what is expected from a damped harmonic oscillator, with a pseudo-pulsation $\omega = 3.4 \pm 0.1 \text{ s}^{-1}$, and an exponentially decaying envelop (dotted line) $A e^{-t/\tau}$, with $A = 2.9 \pm 0.1$ cm and $\tau = 5.4 \pm 0.2$ s.

the particle, relative to the film centre, are plotted in blue and orange in figure 1(c) as a function of time t . They exhibit damped harmonic oscillations with a nearly identical period but different amplitudes, due to the nature of the trajectory. The position of the particle along the primary direction of the spiral is fitted by a damped sinusoidal function of the form $A \exp(-t/\tau) \sin(\omega t + \phi)$, with A and ϕ two constants. In figure 1(c), the pseudo-pulsation is $\omega = 3.4 \pm 0.1 \text{ s}^{-1}$ and the characteristic time of the exponential envelope (shown with a dotted line) is $\tau = 5.4 \pm 0.2$ s. Damped oscillations are observed for all the particles that were tested (e.g. see supplementary movies 2 and 3). Their presence indicate that, at the dominant order, the particle is (i) driven by a spring-like force $\mathbf{F} = -k(\mathbf{x} + \mathbf{y}) = -k\mathbf{r}_m$ (with k the spring constant and \mathbf{r}_m the radial distance between the bead and the film centres) and (ii) slowed down by a viscous drag force $\mathbf{F}_{friction} = -\alpha\mathbf{v}$ (with α the friction coefficient and \mathbf{v} the particle velocity). The friction coefficient $\alpha = 2m/\tau$ and the spring constant $k = m[\omega^2 + (1/\tau^2)]$ are deduced from ω and τ using a damped harmonic oscillator model. Here m is the effective mass of the moving object, taking into account the added mass of the meniscus around the particle.

With the reflective lighting used here (where the soap film acts as a mirror reflecting light to the camera), the meniscus appears as a darker area surrounding the particle in the top-view images. Its size R increases over the course of the oscillations from $R = 2.05 R_b$ (relative to the centre of the particle) at $t = 0$ to $3.63 R_b$ after 30 s in figure 1(b). The curve $R(t)$ is presented in figure 5(b) (Appendix A). The density of the particles being significantly higher than that of the film, the meniscus growth causes a modest variation of the effective mass m with time: in figure 1(b) (and later in figure 5b), m varies from $1.08 m_b$ at $t = 0$ to $1.24 m_b$ at $t = 30$ s. Experimentally, α and k are calculated from a fit over the duration of the oscillations: the value obtained is therefore a time average between the start and end of the oscillations. For this reason, we also use an average effective mass m for the moving object. In practise, m is measured at a time $t = 2.5\tau$, corresponding to half of the oscillation duration (green dotted line in Appendix A, figure 5b). As shown later in figure 5(c), m is typically 20 % higher than the mass m_b of the particle alone.

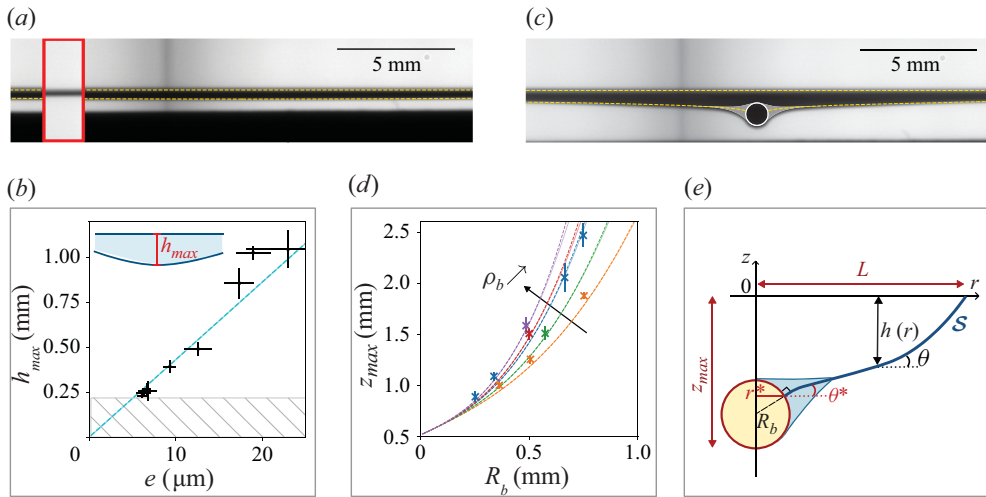


Figure 2. (a) Side-view image of a soap film attached to a frame of size $2L = 6.7$ cm, evidencing the film deformation under its weight. The dotted line is the full numerical solution of the film shape. The inset (in red) is a picture of the frame without the film. (b) Maximum deformation h_{max} of the film as a function of its thickness e . The hatched area is a region where h_{max} cannot be measured. Equation (3.3) is shown with a continuous line; the numerical solution is a perfectly superposed dotted line. (c) Deformation of the film in the presence of a marble of radius $R_b = 0.5$ mm (with theoretical position shown with a white circle). The dotted line is the numerical solution of the film shape; the meniscus shape is added in grey. (d) Maximum deformation z_{max} as a function of R_b . The experiments are shown with crosses, for varying ρ_b : 2580 kg m^{-3} (orange), 4100 kg m^{-3} (green), 6300 kg m^{-3} (blue), 7100 kg m^{-3} (red) and 9200 kg m^{-3} (purple) and compared with 3.4 (continuous lines). The numerical solution is shown with a dotted line. The best fit is obtained for $e = 12 \text{ }\mu\text{m}$. (e) Notations used to model the film shape.

In the rest of the paper, we systematically take into account the added mass of the meniscus and use the effective mass m for the particle.

To model the particle dynamics, we first study in § 3 the film deformation, which is then used in § 4 to model the spring force. In § 5, we finally characterise the friction force.

3. Film deformation by a static particle

The film deformation is observed from the side using a back-light illumination. The light source (a square LED light of width 50 cm and height 25 cm) is placed 2 m away from the film, and a vertical plate with a slit of height 1 cm is positioned a few centimetres in front of the frame. This set-up ensures that the incident light rays on the film are almost parallel, with a variation of incident angles smaller than 3 degrees. The soap film, consisting of two parallel interfaces, does not deflect the light. However, a large majority of the light intensity is reflected when the film is illuminated by a grazing light: a darker area is then visible on the camera sensor, corresponding to the projection of the film shape in the (y, z) plane. The frame used here is a nylon wire of diameter $120 \text{ }\mu\text{m}$ held between four vertical posts. It appears as a fuzzy grey line of width $220 \text{ }\mu\text{m}$. It is shown (in absence of a film) in the inset of figure 2(a) (red rectangle), with the same scale and position as the rest of the picture.

Figure 2(a) shows an image of a film of size $2L = 6.7$ cm obtained with this method (the black area below the film is the edge of the slit). The dark region induced by the reflection of the ray lights on the film is $393 \pm 35 \text{ }\mu\text{m}$ thick: it is much larger than the film thickness ($e = 10 \text{ }\mu\text{m}$) or the apparent frame diameter (red inset), indicating

that the film is deflected. In figure 2(b), the maximum deflection of the film h_{max} is measured for various film thicknesses e , obtained by puncturing the film. The error bars show the standard deviation of 10 experiments, and the hatched area indicates the region where the film shadow is smaller than the apparent diameter of the frame. The amplitude of the deflection h_{max} increases linearly with e ; it reaches 1 mm for the thicker films ($e = 23 \mu\text{m}$). Figure 2(c) is a picture of the film of figure 2(a), now holding a marble of radius $R_b = 0.5 \text{ mm}$ and density $\rho_b = 9200 \text{ kg m}^{-3}$ (which theoretical position is highlighted by a white circle). The marble induces an additional deformation of the order of the initial film deflection. To characterise it, we plot in figure 2(d) the maximum deflection z_{max} measured as the distance between the top of the film and the bottom of the marble. We vary both the bead radius R_b and its density ρ_b . The crosses are the experimental measurements, and the dotted lines show (3.4). The deflection z_{max} increases both with R_b and ρ_b , with an offset of $530 \mu\text{m}$ for $R_b = 0$ associated with the film deformation in absence of a particle.

The film geometry is determined using an axisymmetric model, thus assuming a circular frame. The film height is noted $h(r)$ with r the distance to the centre of the film in cylindrical coordinates, in the (x, y) plane of the frame. The film is identified with the surface S given by $z = h(r)$ (see figure 2(e) for a definition of the variables). Close to the bead, the two film interfaces separate to form a meniscus: in that region, S (shown as a dark blue line in figure 2e) is the midsurface between the two interfaces. As the particle is entirely wet, S is perpendicular to the solid along the contact line, located at $r = r^* = R_b \cos \theta^*$, with θ^* the angle between the normal to the particle and the horizontal at the contact line. Here θ^* is given by the vertical equilibrium between the surface tension force and the particle's weight: $2 \times 2\pi \gamma r^* \sin \theta^* = mg$ so that $\sin(2\theta^*) = mg / (2\pi \gamma R_b)$. The condition $\sin(2\theta^*) \leq 1$ sets the criteria at which a particle of mass m (density ρ_b) and radius R_b can be held within the soap film. For $\rho_b = 6300 \text{ kg m}^{-3}$, the critical bead radius predicted by the theory is $R_{c,th} = 0.90 \text{ mm}$. This is consistent with our experimental observations, where $0.75 < R_c < 1.05 \text{ mm}$.

The film shape $h(r)$ is determined by the force balance on a film element, projected on its normal, where the Laplace pressure due to the two curved liquid interfaces $2\gamma\kappa$ (with κ the local curvature of the film) balances that of the weight of the film $\rho g e \cos \theta$ (with θ the angle between the tangent to the film and the horizontal, or equivalently between the normal to the film and the horizontal). The equation $\kappa = \rho g e \cos \theta / (2\gamma)$ is solved numerically using the same parametrisation as Cohen *et al.* (2017), and the predicted film shape is shown with dotted lines in figures 2(a) and 2(c). It matches well the film distortion, with the film thickness as an adjustable parameter. The best fit is obtained for $e = 11 \mu\text{m}$, which corresponds to the film calibration: $e = 9.8 \pm 1.4 \mu\text{m}$. In our experiments, $\|\nabla h\| \sim h_{max}/L \simeq 10^{-2} \ll 1$, meaning that the problem can be simplified to a small deflection situation and solved analytically. The curvature of the film is then $\kappa = \Delta h$ and $\cos \theta \simeq 1$ so that $h(r)$ is the solution of

$$\Delta h = \frac{\rho g e}{2\gamma}. \tag{3.1}$$

For a particle placed at the centre of the film, (3.1) is solved with the following constraints: (i) the film is attached to the frame, so that $h = 0$ in $r = L$ and (ii) it is attached to the particle in $r = r^* = R_b \cos \theta^* = R_b$. For small deflections, the attachment condition simplifies to $dh/dr|_{r=R_b} = \theta^* = mg / (4\pi \gamma R_b)$. The physical boundary condition of a $\pi/2$ contact angle between the mid plane of the film and the bead is replaced in this limit by a condition of contact along the bead diameter at a free angle; an approximation that we

will keep in the following models. The film shape is then

$$h(r) = \frac{mg}{4\pi\gamma} \ln \frac{r}{L} + \frac{\rho g e}{8\gamma} (r^2 - L^2), \quad (3.2)$$

with the approximation that $\rho\pi R_b^2 e \ll m$. Due to the linearity of (3.1), $h(r)$ is the sum of a logarithmic deformation caused by the particle mass and a parabolic deformation due to the film mass. The maximum deflection of the film is then deduced directly from (3.2):

$$h_{\max} = \max(|h|) = \frac{\rho g e L^2}{8\gamma} \text{ in absence of the bead} \quad (3.3)$$

$$\text{and } z_{\max} = \frac{mg}{4\pi\gamma} \ln \frac{r}{L} + \frac{\rho g e}{8\gamma} (L^2 - R_b^2) + R_b \left(1 + \frac{mg}{4\pi\gamma R_b} \right) \text{ with the bead.} \quad (3.4)$$

Equation 3.3 is shown with a continuous line in figure 2(b): the small deflection approximation perfectly overlaps the complete numerical solution of the problem (dotted line). It also fits the experimental measurements without an adjustable parameter. A good fit between (3.4) (continuous line) and the experiments is also observed in figure 2(d). A small difference between the linearised solution and the complete numerical solution (dotted lines) is visible for the largest R_b , but it remains much smaller than the experimental error bars. Here, the best fitting parameter is $e = 12 \mu\text{m}$, a value close to the calibration of the film thickness.

4. Film force on a bead

The force exerted by the film on the bead can be decomposed into two components. The vertical component, F_{\perp} , holds the particle in the film by counterbalancing its weight: $F_{\perp} = mg$. The in-plane component, F , drives the motion of the particle (figure 1b). In the following, we focus the characteristics of the in-plane force, F .

The force F is first measured in static conditions, by tilting the frame at an angle β . Here, β is kept small enough (below one degree) that, in the absence of a particle, the film retains its parabolic shape. When the frame is tilted, the particle stabilises at a position r_m where the film force F balances the projection of the weight of the particle in the (x, y) plane $mg \sin \beta$ (see the inset of figure 3a). In figure 3(a), the equilibrium position r_m is plotted as a function of the tilt angle $\sin \beta$ for three beads with effective mass $m = 0.75 \text{ mg}$ (blue), $m = 2.05 \text{ mg}$ (orange) and $m = 5.04 \text{ mg}$ (green). The equilibrium position of the particle does not depend on m , as evidenced by the collapse of the data. In addition, r_m increases linearly with $\sin \beta$, which indicates that the in-plane film force on the bead, $F = mg \sin \beta$, is linear in the domain where it is measured (75 % of the width of the frame). This is consistent with the particle dynamics in a horizontal frame, where a linear spring force $F = kr_m$ is deduced from damped harmonic oscillations. In figure 3(b), the spring coefficient k is plotted as a function of the effective mass m . Here, k is determined from tilting the film (blue dots) and from the particle oscillations (red dots). In both cases, k increases linearly with m (which is varied by a factor $\simeq 20$ between 0.5 mg and 13.4 mg). Note that two different frames are used in these experiments (a nylon wire frame of size $2L = 6.7 \text{ cm}$ for the blue points and a 2 mm thick frame with $2L = 10 \text{ cm}$ for the red points), so that the exact values of k cannot be directly compared.

To model this spring force, the film-shape equation (3.1) has to be solved for a particle off-centred by a distance r_m . Due to the linearity of (3.1), the film deformation h is the superposition of (i) the deformation caused by the weight of the film $h_1 = \rho g e (r^2 -$

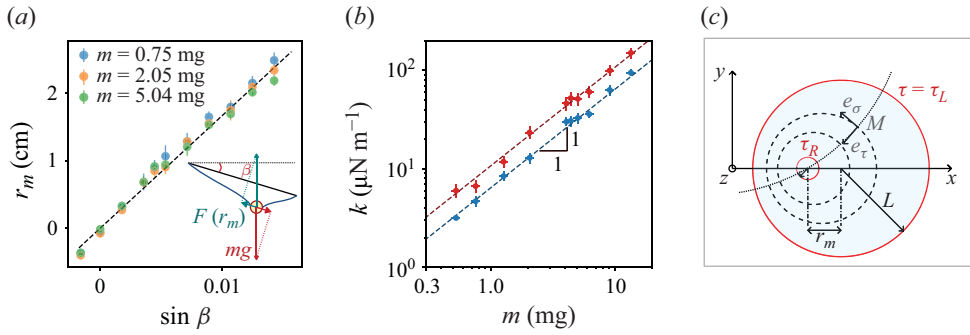


Figure 3. (a) Equilibrium position r_m of the particle as a function of the tilt angle $\sin \beta$. The experiments are shown with dots (blue, $m = 0.75$ mg; orange, $m = 2.05$ mg; green, $m = 5.04$ mg); the error bars are the standard deviation of 10 measurements. The dotted line shows (4.1), with fitting parameter $e = 8.0 \mu\text{m}$. The inset is a schematic of the tilted frame experiment. (b) Spring constant k as a function of the effective mass m (static measurements in blue, dynamic measurements in red). Equation (4.1) is shown with dotted lines, with fitting parameter $e = 8.9 \mu\text{m}$ for the static experiment (blue) and $e = 14.2 \mu\text{m}$ for the dynamic experiment (red). In both cases, the fitting parameter matches the film thickness calibration (two different frames are used). (c) In bipolar coordinates, any point M of the plane has coordinates (σ, τ, z) with an orthonormal basis $(\mathbf{e}_\sigma, \mathbf{e}_\tau, \mathbf{e}_z)$. The iso- τ curves are non-intersecting circles: the circular frame is defined by $\tau = \tau_L$ and the equator of the particle is $\tau = \tau_R$ (both shown in red).

$L^2)/(8\gamma)$, as previously determined (3.2) and (ii) the deformation h_2 of a weightless film subjected only to the weight of an off-centred particle. We start by calculating the force that the deformation h_1 alone would create. In this limit, the film shape does not depend on the bead position and its surface energy is constant. The particle is held by the film at a height $z = h_1(r_m)$: it is thus in a potential well of equation $E = mgz$. This produces a horizontal spring force of amplitude $F_1 = |-\partial E/\partial r_m|$:

$$F_1 = \frac{m\rho e g^2}{4\gamma} r_m. \tag{4.1}$$

Interestingly, the force F_1 alone reproduces remarkably well the experimental data. First, similarly to what is expected of a particle in a tilted bowl, the equilibrium position of the bead varies linearly with the tilt angle $\sin \beta$ and does not depend on the mass of the particle. In figure 3(a), $r_m = f(\sin \beta)$ is fitted by a linear curve of slope $4\gamma/(\rho g e)$, as expected from (4.1), with $e = 8.0 \mu\text{m}$ as a fitting parameter (dotted line). More importantly, (4.1) reproduces the linearity of F with the effective mass m for both static and dynamic experiments, as evidenced in figure 3(b). The best fit is $e = 8.9 \mu\text{m}$ for the static measurements and $e = 14.2 \mu\text{m}$ for the dynamic experiments. Both values match the film thickness calibration with the two different frames: $e = 9.8 \pm 1.4 \mu\text{m}$ for the blue points and $e = 14.6 \pm 2.3 \mu\text{m}$ for the red points. Experimentally, the particle moves as if it were trapped in a parabolic well only determined only by the mass of the film. The catenoid-like film deformation induced by the particle does not impact its dynamics, even if h_1 and h_2 are of the same order of magnitude (figures 2b and 2d).

To understand this apparent discrepancy, we calculate the force F_2 due to h_2 only (corresponding to the limit of a particle in a weightless film). Here F_2 is found by solving the film-shape equation $\Delta h_2 = 0$ for an off-centred particle in the small deflection limit. The boundary conditions are $h_2 = 0$ at the frame and $h_2 = h_R$ at the equator of the particle ($h_R = f(r_m)$) is the vertical position of the centre of the particle, calculated later). In this problem, a relevant coordinate system are bipolar coordinates (σ, τ, z) ,

shown in figure 3(c). In bipolar coordinates, the circular frame is expressed simply as the iso- τ curve $\tau = \tau_L$ and the equator of the particle as $\tau = \tau_R$ (see Appendix B). Solving the film equation in bipolar coordinates becomes straightforward, and gives $h_2 = h_R(\tau - \tau_L)/(\tau_R - \tau_L)$. The film deformation is associated with the surface energy $E_\gamma = E_0 + 2\pi\gamma h_R^2/(\tau_R - \tau_L)$ where E_0 is the surface energy of the flat film in the absence of a particle. The force F_2 is calculated from the total energy $E = E_\gamma + mgh_R$ of the system {particle + film}. First, the vertical equilibrium of the particle imposes $\partial E/\partial h_R = 0$, which gives the vertical position of the particle $h_R = -mg(\tau_R - \tau_L)/(4\pi\gamma)$. Using the expression of h_R , E writes $E = E_0 - (mg)^2(\tau_R - \tau_L)/(8\pi\gamma)$. When expressed in cylindrical coordinates, E is a harmonic (see Appendix B), but it is harmonic in the limit $r_m \ll L$: $E \simeq E_1 + (mg)^2 r_m^2/(8\pi\gamma L^2)$, where $E_1 = E_0 - (mg)^2/(8\pi\gamma) \ln(L/R)$ is the surface energy of the film when the marble is centred. Finally, the amplitude of the film force F_2 is calculated as $F_2 = |-\partial E/\partial r_m|$, which writes

$$F_2 = \frac{(mg)^2}{4\pi\gamma L^2} r_m. \quad (4.2)$$

The film force (F_2) increases quadratically with the mass m of the particles, which differs from the experiments where $F \propto m$ (figure 3b). This confirms that F_1 dominates: the key factor in the particle dynamics is the deformation of the film under its weight.

This is understood by calculating the ratio of the two forces $F_1/F_2 = \rho\pi L^2 e/m$, which is the exact ratio of the masses of the film and the particle. In our experiment, the mass of the film m_{film} is close to 35 mg: it is 3–100 times higher than the particle mass, explaining why F_1 dominates. By keeping the same film size, and in the limit of small, dense particles such as those used here ($R_b \ll L$ and $\rho_b > \rho$) the condition $F_1 > F_2$ is almost always verified. Taking, for example, $\rho_b = 5000 \text{ kg m}^{-3}$, the maximum bead mass that can be held by the film is $m_{max} = 19 \text{ mg}$ (see § 3), which is still smaller than the mass of the film. However, the force F_2 is expected to dominate when reducing the film size L : for a particle of mass $m = 5 \text{ mg}$, it happens for $L < 1.8 \text{ cm}$. Experimentally, we could not test this limit due to edge effects (the bead is attracted towards the frame by capillarity at distances of the order of 5 mm).

5. Friction in a soap film

We finally focus on the friction force $F_{friction} = -\alpha\mathbf{v}$ (with \mathbf{v} the particle velocity) experienced by the particle during its motion. The friction coefficient α is deduced from the characteristic time τ of the exponential envelope of $x(t)$ and $y(t)$ (figure 1c), using a damped harmonic oscillator model. Due to the extending meniscus around the particle (see figure 5 in Appendix A), we expect α to vary with time as the effective radius of the particle increases. Experimentally, this variation is small enough not to significantly perturb exponential fit. In figure 4(a), α is plotted as a function of the radius R_b of the particle; the different colours correspond to different particle densities ρ_b . The friction coefficient is extremely small: $\alpha \simeq 1 \text{ }\mu\text{Pa s m}$ for a millimetre-sized particle. This is of the order of the drag experienced by Leidenfrost droplets (Quééré 2013) and 10 times smaller than the friction of a particle floating at the surface of a bath of bulk viscosity η , where $\alpha \simeq 3\pi\eta R \simeq 10 \text{ }\mu\text{Pa s m}$ (Danov, Dimova & Pouligny 2000).

To understand and model the friction coefficient α , one must first consider the flow (in the film and in the air) induced by the translation at a velocity v of a particle trapped in the film (figure 4b).

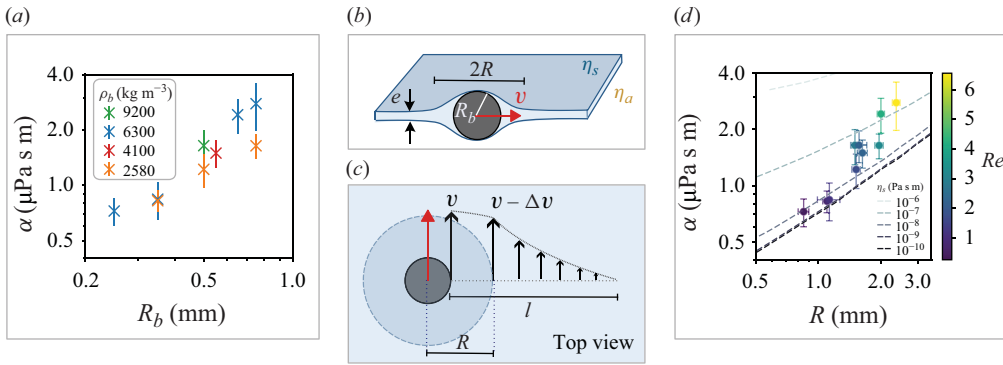


Figure 4. (a) Translational drag coefficient α as a function of the radius R_b of the particle, for varying marble densities. (b) Side view of a particle immersed in a soap film. (c) Top view. The limit of the meniscus surrounding the particle is shown with a dotted blue line. The arrows evidence the shear flow in the meniscus and the film. (d) Comparison between model and experiments for the drag coefficient α as a function of the effective radius R of the moving object (particle + meniscus). The colour code shows the Reynolds number (in air) for each experiment. The dotted lines show the theory for varying surface viscosities η_s , from 10^{-6} Pa s m (light grey) to 10^{-10} Pa s m (black). The curves for 10^{-9} Pa s m and 10^{-10} Pa s m are almost perfectly superimposed.

In the film, the total flow is the sum of the flow towards the bead by capillary suction (with characteristic velocity v_c) and the flow induced by the translation of the particle. The value of v_c is first estimated from the variation $\Delta\Omega \simeq 4R_b^3$ of the meniscus volume in the duration $\Delta t \simeq 30$ s of an experiment (see figure 5b). It gives $v_c = (\Delta\Omega/\Delta t) \times 1/(e2\pi R) \simeq 500 \mu\text{m s}^{-1}$, which is more than 10 times smaller than v . The flow induced by capillary suction is therefore negligible compared with the flow induced by the motion of the bead.

Due to the mobility of the interfaces, the velocity field induced by the motion of the particle is dominated by in-plane flows, which are invariant along the z -direction. Figure 4(b) is a sketch from the top of the experiment, where the velocity profile $v = v_\theta(r)$ of the in-plane flow perpendicular to the direction of motion of the particle is shown with black arrows. Here, the shear happens over a characteristic distance l of the order of a few times R_b (Stone & Ajdari 1998). If we now focus on the viscous dissipation associated with the in-plane flow, a two-dimensional (2-D) apparent viscosity term appears: $\eta^{2D} = 2\eta_s + \eta e$, which is the sum of (i) the surface viscosity η_s associated with the shearing of the 2-D surfactant-rich layers at the two-liquid–air interfaces and (ii) the liquid bulk viscosity integrated over the thickness e of the film, ηe . The measurement of the surface viscosity of interfaces populated by soluble surfactants such as SDS has demonstrated to be particularly challenging (Stevenson 2005). However, a carefully designed experiment of Zell *et al.* (2014) gave an upper bound $\eta_s < 0.01 \mu\text{Pa s m}$. Here, ηe is systematically higher than this value: in a first approximation, we therefore consider that $\eta^{2D} \simeq \eta e$. The validity of this assumption, and the impact of η_s on the friction is discussed later.

An important parameter for the friction is the presence of the meniscus surrounding the particle. It creates a region of characteristic size R (see figure 5a in Appendix A) where the film thickness is $\sim R_b$, which is 100 times thicker than the rest of the film. To evaluate the impact of the presence of a thicker zone on the in-plane flows, we calculate the velocity $v - \Delta v$ of the fluid in the film at the boundary between the meniscus (dark blue in figure 4c) and the film (light blue) using a scaling law analysis. For simplicity, we consider that the film thickness is uniform in the meniscus and suddenly decreases from R_b

to e at the boundary, i.e. at a distance $R - R_b \sim R_b$ from the equator of the particle. This induces a jump of the 2-D viscosity, from $\eta^{2D} \sim \eta R_b$ in the meniscus to $\eta^{2D} \sim \eta e$ in the film. The continuity of the surface stress $\sigma^{2D} = \eta^{2D}(\partial v/\partial r)$ (the shear stress integrated over the film thickness) then gives Δv . Using the notations of figure 4(b), σ^{2D} scales as $(\eta R_b)\Delta v/R_b$ in the meniscus, and $(\eta e)(v - \Delta v)/l$ in the film. Equating these two terms gives $\Delta v \sim (e/l)v$ and $v - \Delta v \sim (1 - e/l)v \simeq 0.99v$, meaning that the meniscus moves with the particle at a velocity v . In addition, in the absence of a velocity gradient, there is no viscous dissipation in the meniscus. From the outside, the particle and its meniscus thus form a larger object with effective radius R and effective mass m . Similarly to what is done for m , the characteristic dimension R is measured for each experiment at a time $t = 2.5\tau$ corresponding to half of the duration of the oscillations.

The translation of the particle and the meniscus also induce a shear flow in the surrounding air. The Reynolds number associated with this motion writes $Re = \rho_a R v / \eta_a$, with, respectively, ρ_a and η_a the density and viscosity of air. We take the characteristic velocity v as the average maximum velocity of the particle over the duration of the oscillations. Experimentally, Re varies between 0.25 for the smallest (and slowest) particle and 6.5 for the larger one. The smallest particles thus induce a Stokes flow in the air, while for the largest particles, a visco-inertial boundary layer starts to develop. Inertial effects are expected to impact the friction: for a sphere translating in air, the friction coefficient is increased by 50% at $Re = 6$ compared with the Stokes drag (Munson, Young & Okiishi 1995).

In the following, we propose to model the friction in the (simpler) situation of $Re < 1$. In this regime, the relative contributions of the film and the surrounding air to the viscous dissipation are given by the Boussinesq number $Bo = (\eta e + 2\eta_s)/(\eta_a R)$. For a characteristic film thickness $e = 10 \mu\text{m}$, $Bo \simeq 2$: a value close to one, meaning that the bulk film and air both contribute to the friction. This configuration has been rarely considered in the literature, which is generally focused on the $Bo \ll 1$ limit (the drag of an object in a three-dimensional fluid) and $Bo \gg 1$ (an inclusion trapped in a viscous membrane). We propose here to base our analysis on the prediction of Hughes, Pailthorpe & White (1981), who solved numerically the translational drag coefficient α of a non-protruding cylindrical inclusion in a membrane for any arbitrary Boussinesq number. They show that, for an inclusion of radius R , the friction coefficient writes $\alpha = 8\pi\eta_a R \Lambda_T(Bo)$ with $\Lambda_T(Bo)$ a numerical coefficient decreasing when the Boussinesq number increases. In our system, however, the particle with radius $R_b \gg e$ protrudes strongly from the film. To account for this, we consider in a first approximation that the friction of the marble and meniscus in a soap film is equal to the friction of a disk of radius R in a membrane surrounded by air (Hughes *et al.* 1981) to which we add the difference between the friction of a sphere of size R in air ($\alpha = 6\pi\eta_a R$) and that of an infinitely thin disk moving in its plane direction ($\alpha = 32\eta_a R/3$) (Happel & Brenner 1983). This gives the following expression for α :

$$\alpha = 8\pi\eta_a R \left[\Lambda_T \left(\frac{\eta e + 2\eta_s}{\eta_a R} \right) + \frac{3}{4} - \frac{4}{3\pi} \right]. \quad (5.1)$$

In figure 4(d), the experimental measurement of α is plotted as a function of the effective radius of the moving object R . The colour code indicates the Reynolds number in air, varying from $Re = 0$ (dark blue) to $Re = 6.5$ (yellow). The dotted lines are the theoretical prediction for varying surface viscosities η_s , varied logarithmically between 10^{-10} (black) and 10^{-6} (light grey). For the smallest particles ($R < 2 \text{ mm}$ and $Re < 1$), the measured friction coefficient α matches the prediction of (5.1), for a surface viscosity $\eta_s \leq 10^{-8} \text{ Pa s m}$. These values of the surface viscosity agree perfectly with the previous

measurement of Zell *et al.* (2014), who also gave 10^{-8} Pa s m as an upper boundary for the surface viscosity. As the Reynolds number increases, the experiments deviate from the theoretical curve: the friction coefficient α is higher than that expected from a model based on purely viscous flows. An increase of α is coherent with inertial effects; however, there is no simple way to simply model it as the friction coefficient results from a complex interplay between the flow in the film and in air (Hughes *et al.* 1981).

6. Conclusion

To conclude, we measured and modelled the forces that apply to a millimetre-sized particle trapped in a soap film, by focusing on both the static position of the bead and its motion. We show that the gravitational distortion of the film under its own weight – of only a few hundreds of micrometres – is the key to understanding the bead dynamics. Indeed, in our experiment, the component of the force due to the film weight systematically dominates over the force induced by the weight of the particle. This is expected as long as the mass of the film is larger than the mass of the particle, which happens for solid particles of size $R \ll L$. Counter-intuitively, decreasing the size of the film while keeping the same ratio between the particle radius and the film width $L/R \simeq 100$ will only increase the relative importance of the film weight. For example, for a $10\ \mu\text{m}$ particle trapped on an $1\ \text{mm}^2$ horizontal film, $F_1/F_2 > 10$ even for very thin films of $e \simeq 100\ \text{nm}$.

In the second part, we focus on the drag force experienced by the particle, and we propose a model in the limit of low Reynolds number in air ($Re < 1$). In this regime, the particle is submitted to the viscous friction of air and to that of the film, with an almost equal contribution. A simplified model based on the work of Hughes *et al.* (1981) matches exactly our measurements for the smallest particles. A deviation is observed as the Reynolds number (and the size of the particle) increase, which we interpret as the effect of the inertia of the air. Interestingly, the match between the theory and the experiments is valid for all surface viscosities $\eta_s \leq 10^{-8}$ Pa s m: a mismatch of at least 50 % is expected for $\eta_s \geq 10^{-7}$ Pa s m. This suggests that our experiment should be sensitive to surface viscosities as low as 10^{-8} Pa s m, which is as sensitive as the most precise interfacial rheology set-ups, for example controlled microrheological probes at the surface of a bath (Zell *et al.* 2014). We expect our model to remain valid when reducing the size of the probe, which opens interesting perspectives on the possibility of using small particles as probes to explore in-situ the rheological properties of soap film.

Supplementary movies. Supplementary movies are available at <https://doi.org/10.1017/jfm.2025.157>.

Acknowledgements. The authors thank D. van der Meer for the initial discussions on the topic, and M. Taoufiki and H. Delrieu for preliminary experiments.

Declaration of interests. The authors report no conflict of interest.

Appendix A. Meniscus characterisation

A particle trapped in a soap film is surrounded by a meniscus which extends with time by capillary suction. Figure 5 characterises the shape of the meniscus, and presents its growth dynamics in a typical experiment. The presence of the meniscus increases the effective mass m of the moving object, which is taken into account in the calculation of the forces.

Appendix B. Calculation of the film-mediated force in bipolar coordinates

We want to determine the energy of the system consisting of a particle of radius R_b off-centred by r_m in a circular soap film of radius L . In bipolar coordinates, any point M has

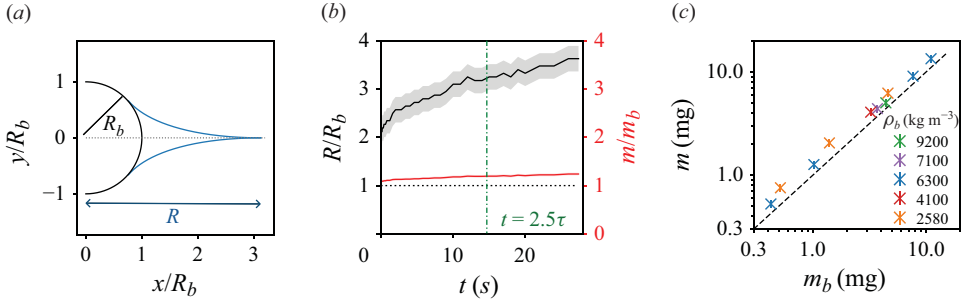


Figure 5. (a) Shape of a meniscus with an extension $R = 3R_b$ around a particle, calculated based on Orr *et al.* (1975). The position of the interface is normalised by the particle radius R_b . (b) Normalised extension R/R_b of the meniscus (black line) and mass m/m_b (red line) as a function of time t , for a particle of radius $R_b = 0.5$ mm and mass $m_b = 3.7$ mg. The black dotted line evidences the limit $R = R_b$ and $m = m_b$. The vertical green line evidences the time $t = 2.5\tau$ at which the characteristic size R and mass m are measured. Here $t = 2.5\tau$ is half of the duration of the oscillations. (c) Total mass m of the particle and its meniscus, measured at a time $t = 2.5\tau$, as a function of the mass m_b of the particle alone. The dotted line shows the limit $m = m_b$.

coordinates (σ, τ, z) . The iso- τ curves are circles of radius $c/|\sinh \tau|$, centred in $(x = c \coth \tau, y = 0)$, with c a constant, and the iso- σ curves are circles of radius $c/|\sin \sigma|$, centred in $(x = 0, y = c \cot \sigma)$. One needs to find the constant c so that the frame position is expressed simply as $\tau = \tau_L$ and the edge of the particle is $\tau = \tau_R$ (as shown in figure 3c). We can restrict τ_L and τ_R to be positive, and by construction of the bipolar coordinates, $\tau_R > \tau_L$. The relation between τ_L, τ_R, c and the dimensions of the problem L, R_b and r_m is solved by inverting the three relations $r_m = c(\coth \tau_L - \coth \tau_R)$ ($r_m > 0$), $L = c/\sinh \tau_L$ and $R_b = c/\sinh \tau_R$. In particular,

$$\cosh \tau_L = \frac{L^2 - R_b^2 + r_m^2}{2Lr_m} \text{ and } \cosh \tau_R = \frac{L^2 - R_b^2 - r_m^2}{2Rr_m}. \quad (\text{B1})$$

In bipolar coordinates, $\Delta h = (\cosh \tau - \cos \sigma)^2 (\partial^2 h / \partial \sigma^2 + \partial^2 h / \partial \tau^2) / c^2$ (Happel & Brenner 1983). The film-shape equation $\Delta h_2 = 0$ is then solved with the boundary conditions $h(\tau_L) = 0$ and $h(\tau_R) = h_R$, giving a simple solution: $h_2 = h_R(\tau - \tau_L) / (\tau_R - \tau_L)$. In the small deflection limit, the surface energy associated with the film deformation is $E_\gamma \simeq E_0 + \gamma \iint (\nabla h)^2 dS$. A small surface element is $dS = c^2 d\sigma d\tau / (\cosh \tau - \cos \sigma)^2$ while $\nabla h = (\cosh \tau - \cos \sigma)(\mathbf{e}_\sigma \partial h / \partial \sigma + \mathbf{e}_\tau \partial h / \partial \tau) / c$. Using the expression of h_2 , the film energy is

$$E_\gamma = E_0 + \gamma \int_0^{2\pi} d\sigma \int_{\tau_L}^{\tau_R} \left(\frac{\partial h_2}{\partial \tau} \right)^2 d\tau = E_0 + 2\pi\gamma \frac{h_R^2}{(\tau_R - \tau_L)}. \quad (\text{B2})$$

The total energy E of the film and particle is $E = E_\gamma + mgh_R$. The vertical equilibrium of the particle imposes $\partial E / \partial h_R = 0$, which gives $h_R = -mg(\tau_R - \tau_L) / (4\pi\gamma)$ and $E = E_0 - (mg)^2(\tau_R - \tau_L) / (8\pi\gamma)$. Using (B1), and in the limit $R_b \ll L$, E finally writes

$$E = E_0 - \frac{(mg)^2}{8\pi\gamma} \left[\ln \frac{L}{R_b} + \ln \left(1 - \frac{r_m^2}{L^2} + \sqrt{1 - 2\frac{r_m^2}{L^2}} \right) - \ln \left(1 + \frac{r_m^2}{L^2} + \sqrt{1 - 2\frac{r_m^2}{L^2}} \right) \right]. \quad (\text{B3})$$

REFERENCES

- ALMGREN, F.J. & TAYLOR, J.E. 1976 The geometry of soap films and soap bubbles. *Sci. Am.* **235** (1), 82–93.
- ARADIAN, A., RAPHAËL, E. & DE GENNES, P.G. 2001 Marginal pinching in soap films. *Europhys. Lett.* **55** (6), 834–840.
- CHEN, C.H., PERERA, A., JACKSON, P., HALLMARK, B. & DAVIDSON, J.F. 2019 The distortion of a horizontal soap film due to the impact of a falling sphere. *Chem. Engng Sci.* **206**, 305–314.
- COHEN, C., DARBOIS-TEXIER, B., REYSSAT, É., SNOEIJER, J.H., QUÉRÉ, D. & CLANET, C. 2017 On the shape of giant soap bubbles. *Proc. Natl Acad. Sci.* **114** (10), 2515–2519.
- COURANT, R. 1940 Soap film experiments with minimal surfaces. *Am. Math. Mon.* **47** (3), 167–174.
- COURBIN, L. & STONE, H.A. 2006 Impact, puncturing, and the self-healing of soap films. *Phys. Fluids* **18** (9), 091105.
- CULICK, F.E.C. 1960 Comments on a ruptured soap film. *J. Appl. Phys.* **31** (6), 1128–1129.
- DANOV, K.D., DIMOVA, R. & POULIGNY, B. 2000 Viscous drag of a solid sphere straddling a spherical or flat surface. *Phys. Fluids* **12** (11), 2711–2722.
- FELL, D., SOKULER, M., LEMBACH, A., EIBACH, T.F., LIU, C., BONACCURSO, E., AUERNHAMMER, G.K. & BUTT, H.J. 2013 Drop impact on surfactant films and solutions. *Colloid Polym. Sci.* **291** (8), 1963–1976.
- GILET, T. & BUSH, J.W.M. 2009 The fluid trampoline: droplets bouncing on a soap film. *J. Fluid Mech.* **625**, 167–203.
- GOLDSTEIN, R.E., MOFFATT, H.K., PESCI, A.I. & RICCA, R.L. 2010 Soap-film Möbius strip changes topology with a twist singularity. *Proc. Natl Acad. Sci.* **107** (51), 21979–21984.
- GUO, S., XU, X., QIAN, T., DI, Y., DOI, M. & TONG, P. 2019 Onset of thin film meniscus along a fibre. *J. Fluid Mech.* **865**, 650–680.
- HAPPEL, J. & BRENNER, H. 1983 *Low Reynolds Number Hydrodynamics: with Special Applications to Particulate Media*. Martinus Nijhoff.
- HUGHES, B.D., PAILTHORPE, B.A. & WHITE, L.R. 1981 The translational and rotational drag on a cylinder moving in a membrane. *J. Fluid Mech.* **110**, 349–372.
- LE GOFF, A., COURBIN, L., STONE, H.A. & QUÉRÉ, D. 2008 Energy absorption in a bamboo foam. *Europhys. Lett.* **84** (3), 36001.
- MUNSON, B.R., YOUNG, D.F. & OKIISHI, T.H. 1995 Fundamentals of fluid mechanics. *Oceanogr. Lit. Rev.* **42** (10), 831.
- ORR, F.M., SCRIVEN, L.E. & RIVAS, A.P. 1975 Pendular rings between solids: meniscus properties and capillary force. *J. Fluid Mech.* **67** (4), 723–742.
- PAN, K.L. & LAW, C.K. 2007 Dynamics of droplet–film collision. *J. Fluid Mech.* **587**, 1–22.
- QUÉRÉ, D. 2013 Leidenfrost dynamics. *Annu. Rev. Fluid Mech.* **45** (1), 197–215.
- STEVENSON, P. 2005 Remarks on the shear viscosity of surfaces stabilised with soluble surfactants. *J. Colloid Interface Sci.* **290** (2), 603–606.
- STOGIN, B.B., GOCKOWSKI, L., FELDSTEIN, H., CLAURE, H., WANG, J. & WONG, T.S. 2018 Free-standing liquid membranes as unusual particle separators. *Sci. Adv.* **4** (8), eaat3276.
- STONE, H.A. & AJDARI, A. 1998 Hydrodynamics of particles embedded in a flat surfactant layer overlying a subphase of finite depth. *J. Fluid Mech.* **369**, 151–173.
- TAYLOR, G.I. 1959 The dynamics of thin sheets of fluid. iii. disintegration of fluid sheets. *Proc. R. Soc. Lond. A: Math. Phys. Sci.* **253** (1274), 313–321.
- ZELL, Z.A., NOWBAHAR, A., MANSARD, V., LEAL, L.G., DESHMUKH, S.S., MECCA, J.M., TUCKER, C.J. & SQUIRES, T.M. 2014 Surface shear inviscidity of soluble surfactants. *Proc. Natl Acad. Sci.* **111** (10), 3677–3682.